Multiple Levels of Organization in Amphiphilic Diblock Copolymers Produced by Aqueous ROPISA

Marianna Spyridakou, Ioannis Tzourtzouklis, Robert Graf, Hannah Beauseroy, Colin Bonduelle, Sebastien Lecommandoux, George Floudas

Multiple Levels of Organization in Amphiphilic Diblock Copolymers Produced by Aqueous ROPISA

Marianna Spyridakou,[1] Ioannis Tzourtzouklis,[1] Robert Graf,[2] Hannah Beauseroy,[3] Colin Bonduelle,[3*] Sebastien Lecommandoux,[3*] George Floudas[1,2,4 *]

[1] *Department of Physics, University of Ioannina, P.O. Box 1186, 45110 Ioannina, Greece*

[2] *Max Planck Institute for Polymer Research, Ackermannweg 10, 55128 Mainz, Germany*

[3]*University Bordeaux, CNRS, Bordeaux INP, LCPO, UMR 5629, F-33600 Pessac, France.*

[4] *University Research Center of Ioannina (URCI)-Institute of Materials Science and Computing, 45110 Ioannina, Greece*

*: Corresponding author E-mails:

G.F. gfloudas@uoi.gr, ORCID: 0000-0003-4629-3817

C.B. colin.bonduelle@enscbp.fr, ORCID:

S.L. lecommandoux@enscbp.fr, ORCID:

1. INTRODUCTION

In the effort to design new functional materials with precisely controlled – at the synthesis level – internal dimensions and structures ranging from nanometer to macroscopic scales, synthetic polypeptides play an important role. The latter combine the complexity of biological macromolecules found in nature with the simpler synthetic polymers.[1-9] In this respect, amphiphilic block copolymers based on the well-known synthetic polypeptide poly(γ-benzyl-L-glutamate) (PBLG)[10-14] and the water soluble poly(ethylene glycol) (PEG)[15] have been synthesized and investigated with respect to the self-assembly.[6,16-19] The presence of antagonistic tandem interaction between the two blocks (tendency of PEG to crystallize by chain folding and of PBLG to form α-helical/β-sheet peptide secondary structures, on top nanophase separation) gave rise to several levels of organization and structures of key in the design of new functional materials.

A recent method for producing amphiphilic block copolymers and nanoobjects is polymerization-induced self-assembly (PISA).[20,21] The method affords the *in situ* one-step growth of a living amphiphilic polymer chain during its self-assembly into nanostructures. A variation of the method recently explored is the ring-opening polymerization-induced self-assembly (ROPISA) in aqueous buffer.[22,23] It was employed with PEG-NH_2 macroinitiator and either benzyl-L-glutamate or L-leucine NCA monomers for the synthesis of amphiphilic block copolymers of PEG-*b*-PBLG and PEG-*b*-PLeu. The latter were found to stabilize anisotropic rod-like nanostructures. It was thought that responsible for the different nanostructures were the peptide secondary structures (α-helical/β-sheet for PBLG and PLeu, respectively).

Herein we employ the same diblock copolymers (PEG-*b*-PBLG and PEG-*b*-PLeu) and explore the self-assembly and polypeptide dynamics over different length and timescales, as a function of molar mass and for different annealing and solvent treatment protocols. By employing a combination of static (^{13}C-NMR, X-ray scattering, polarizing optical microscopy), thermodynamic (differential scanning calorimetry), and dynamic (dielectric spectroscopy) probes, we demonstrate a record of six levels of organization only found before in natural materials like tendon.[24] They include (a) secondary structures of the polypeptides (α-helical/β-sheet), (b) the unit cell of PEG crystals, (c) the domain spacing of semicrystalline PEG, (d) the nanophase separation of unlike blocks, (e) an intermediate length-scale of rod-like objects (~ 100 nm in size), and (f) distorted slowly growing anisotropic crystalline superstructures (~ 100 μm).

2. EXPERIMENTAL SECTION

2.1 Synthesis

Typical synthesis procedure of poly(ethylene glycol)-b-poly(γ-benzyl-L-glutamate) PEG_{114}-b-$PBLG_{21}$

In a glove box, the NCA monomer of γ-benzyl-L-glutamate (150 mg, 0.57 mmol) was weighted in a Schlenk tube containing a magnetic stirring bar. The Schlenk is removed from the glove box and cooled on ice. 4mL of an ice-cooled solution of $NaHCO_3$ 0.05M containing the initiator PEG_{5k}-NH_2 (150 mg, 0.03 mmol, [M]/[I] = 19) is added to the BLG-NCA powder under a strong agitation (τs = 7%). The reaction is left to stir 1) first in an ice-cold water bath; 2) then at room temperature overnight. The opalescent dispersion obtained is then transferred to a 3.5 kDa dialysis membrane and dialyzed against deionized water for 2 days. An aliquot is kept for further microscopy imaging and the remaining dispersion is lyophilized. A white powder is obtained with a yield of 85%. According to method described by Grazon *et al.*,[23] a PBLG degree of polymerization was calculated from ^{1}H NMR (N_{PBLG} = 21) (Figure S1) and SEC then provided a number-average molecular weight M_n of 10900 g·mol^{-1} (RI, PS calibration) and $Đ$ = 1.06 (Figure S2).

^{1}H NMR (400 MHz, $CDCl_3$ + 15% TFA, δ, ppm): 7.85 (b, 1H, NH), 7.28 (b, 5H, Ar), 5.08 (q, 2H, CH2), 4.60 (b, 1H, CH), 3.70 (s, 4H, O–CH2CH2), 3.52 (s, 3H, CH3), 2.44 (b, 2H, CH2), 2.11–1.91 (b, 2H, CH2).

A part of the lyophilized powder was then used as such for further analysis. Another part was solubilized in DMF, precipitated in diethyl ether, and dried under vacuum overnight.

Typical synthesis procedure of poly(ethylene glycol)-b-poly(γ-benzyl-L-glutamate) PEG_{228}-b-$PBLG_{23}$.

This copolymer was prepared by the same method as described above for copolymer PEG_{114}-*b*-$PBLG_{21}$ except that the molar mass of PEG-NH_2 was higher (PEG_{10k}-NH_2, 98 mg, 0.01 mmol, [M]/[I] =19). Quantity of BLG-NCA was adjusted (49 mg, 0.19 mmol) as well as $NaHCO_3$ 50mM solution (2 mL) to keep the solid content at 7%. Yield: 83%.

^{1}H NMR (400 MHz, $CDCl_3$ + 15% TFA, δ, ppm): 7.85 (b, 1H, NH), 7.28 (b, 5H, Ar), 5.08 (q, 2H, CH2), 4.60 (b, 1H, CH), 3.70 (s, 4H, O–CH2CH2), 3.52 (s, 3H, CH3), 2.44 (b, 2H, CH2), 2.11–1.91 (b, 2H, CH2).

A PBLG degree of polymerization was calculated from ^{1}H NMR (N_{PBLG} = 23) (Figure S3) and SEC

then provided a number average molecular weight M_n of 21400 g·mol^{-1} (RI, PS calibration) and $Đ$ = 1.05 (Figure S4).

Similarly, a part of the lyophilized powder was used as such for further analysis.

Another part was solubilized in DMF, precipitated in diethyl ether, and dried under vacuum overnight.

Typical synthesis procedure of poly(ethylene glycol)-b-poly(L-Leucine) PEG_{114}-b-$PLLeu_{28}$.

The same procedure was employed and adapted to the NCA monomer of L-leucine (Leu-NCA, 75 mg, 0.48 mmol). PEG_{114}-NH2 (75 mg, 0.015 mmol, [M]/[I] = 32), dissolved in 2 mL of NaHCO3 0.05 M was used as initiator (solid content τ = 7%). Yield: 78%

According to method described by Grazon *et al.*,[23] a PLLeu degree of polymerization was calculated from ^{1}H NMR (N_{PLeu} = 28) (Figure S5) and SEC then provided a number-average molecular weight M_n of 42000 g·mol^{-1} (RI, calibration PMMA) and $Đ$ = 1.05 (Figure S6).

1H NMR (400 MHz, TFA-*d*, δ, ppm): 4.65 (b, 1H, CH), 3.85 (s, 4H, O–CH2CH2), 3.52 (s, 3H, CH3), 1.58 (b, 2H, CH2), 0.91–0.87 (b, 7H, –CH–(CH3)2).

Similarly, a part of the lyophilized powder was used as such for further analysis. Another part was solubilized in DMF, precipitated in diethyl ether, and dried under vacuum overnight.

Typical synthesis procedure of poly(γ-benzyl-L-glutamate) $PBLG_{25}$

BLG NCA (1 g, 3.8 mmol, 50eq) was weighed in a previously flame dried Schlenk in a glovebox under pure argon. The powder was then dissolved in 19 mL of anhydrous DMF (0.6 M) at room temperature. Hexylamine (10 µL, 0.08 mmol,1eq) was added and this was considered starting time of the reaction. The solution was stirred for 3 days at room temperature under argon. FTIR allowed to monitor the reaction completion by monitoring the depletion of the bands at 1859 cm^{-1} and 1787 cm^{-1} characteristic of the C=O stretching of NCAs. The polymer was then recovered by precipitation in diethyl ether, twice, and dried under high vacuum.

Yield: 670 mg*;* 67%, white powder. The degree of polymerization was calculated from ^{1}H NMR (N_{PBLG} = 25) (FigureS7), and SEC provided a number-average molecular weight M_n of 4000 g·mol^{-1} (RI, calibration PS) and $Đ$ = 1.26 (Figure S8).

1H NMR (400 MHz, $CDCl_3$ + 15% TFA, δ, ppm): 0.84 (t, 3H, CH3 hexylamine), 1.24 (br, 6H, CH3-(CH2)3- hexylamine), 1.45 (t, 2H, -CH2-CH2-NH- hexylamine), 1.89-2.09 (m, 2H, CH2), 2.42 (t,

2H, CH2, J=6.8 Hz), 3.2 (m,2H, -CH2-NH- hexylamine), 4.58 (m, 1H, CH), 5.06 (m, 2H, CH2O), 7.24-7.27 (m, 5H, ArH).

Table 1. Molecular characteristics of the investigated copolymers.

Samples	$Đ$	N^{PEG}	$N^{peptide}$	f_{PEG}[a]	w_{PEG}
PEG_{114}-*b*-$PLeu_{32}$ (FD)[b]	1.05	114	32	0.60	0.63
PEG_{114}-*b*-$PLeu_{32}$ (OSP)[c]	1.05	114	32	0.60	0.63
PEG_{114}-*b*-$PBLG_{19}$ (FD)	1.06	114	19	0.52	0.49
PEG_{114}-*b*-$PBLG_{19}$ (OSP)	1.06	114	19	0.52	0.49
PEG_{228}-*b*-$PBLG_{19}$ (FD)	1.05	228	19	0.66	0.63
PEG_{228}-*b*-$PBLG_{19}$ (OSP)	1.05	228	19	0.66	0.63

[a] $\rho_{\mathrm{PEG}}{}^{25} = 1.064\ \mathrm{g \cdot cm^{-3}}$, $\rho_{PBLG}{}^{26} = 1.278\ \mathrm{g \cdot cm^{-3}}$, $\rho_{PLeu}{}^{27} = 1\ \mathrm{g \cdot cm^{-3}}$
[b] FD = freeze drying
[c] OSP = organic solvent precipitation

Methods for polymer characterization:

^{1}H NMR spectra were recorded at room temperature with a Bruker Avance 400 (400 MHz). $CDCl_3$ and TFA-*d* were used as solvent and signals were referred to the signal of residual protonated solvent signals.

Size Exclusion Chromatography (SEC). Polymer molar masses were determined by SEC using dimethylformamide (DMF + LiBr 1 g.L^{-1}) or hexafluoro-2-propanol (HFIP + 0.05% KTFA) as eluent. Measurements in DMF were performed on an Ultimate 3000 system from ThermoFischer Scientific (Ilkirch, France) equipped with a diode array detector (DAD). The system also includes a multiangle light scattering detector (MALS) and differential refractive index detector dRI from Wyatt technology (Santa Barbara CA, USA). Polymers were separated on three Shodex Asahipack gel columns [GF 310 (7.5 × 300 mm**²**), GF510 (7.5 × 300 mm^2), exclusion limits from 500–300 000 Da] at a flowrate of 0.5 mL.min^{-1}. Columns temperature was held at 50 °C. Easivial™ kit of Polystyrene from Agilent (Santa Clara CA, USA) was used as calibration standard (M_n from 162 to 364 000 Da). Measurements in HFIP were performed on an Ultimate 3000 system from Thermoscientific equipped with diode array detector DAD. The system also includes a multi-angles light scattering detector MALS and differential refractive index detector dRI from Wyatt technology. Polymers were separated on two PL HFIP gel columns (300 x 7.5 mm) (exclusion limits from 200 Da to 2 000 000 Da) at a flowrate of 0.8mL/min. Columns temperature was held at 40°C. Easivial kit of PMMA from Agilent was used as the standard.

Transmission Electron Microscopy (TEM). The images were recorded on a Hitachi H7650 microscope working at 80 kV. Samples were prepared by deposing a drop of 0.1 g.L^{-1} NP

dispersion onto a copper grid (200 mesh coated with carbon) and removing excess after 1 min. Grids were negatively stained with 1.2% uranyl acetate.

2.2 Small-Angle X-ray Scattering. Small-angle X-ray scattering (SAXS) measurements were made with the N8 Horizon vertical setup (Bruker), using a 50W CuKα radiation (IμS micro-focus source with integrated MONTEL optics). The diffraction patterns were recorded on the VÅNTEC-500 2D detector (Bruker) at a sample-detector distance of 660 mm. The samples were placed in the form of powder within borosilicate glass capillaries with a diameter of 1 mm. Intensity distributions as a function of the modulus of the scattering vector, $q = (4\pi/\lambda)\cdot\sin(2\theta/2)$, where 2θ is the scattering angle and λ = 0.154 nm is the wavelength, were obtained by radial averaging of the 2D datasets. Temperature-dependent measurements of 1 hour long were made by slowly heating the samples from 303 K to 423 K in 5 K steps – with 1 hour equilibration time at each temperature- and subsequent cooling aiming at obtaining the disorder-to-order temperature.

2.3 Wide-Angle X-ray Scattering. Wide-angle X-ray scattering (WAXS) measurements were performed with a D8 Advance Bruker diffractometer, CuKα (40 kV, 40 mA) radiation, equipped with a secondary beam graphite monochromator (λ = 1.54184 nm). The system employed a Bragg-Brentano geometry in a θ-θ configuration. Patterns were obtained over the range of 2θ from 2 deg to 60 deg in steps of 0.01 deg, and the rate was 2 s per step for all samples. The recorded intensity distributions are presented as a function of the modulus of the scattering vector. Scattering curves were taken at a temperature of 303 K.

2.4 Solid-State NMR.

2.5 Polarizing Optical Microscopy. A Zeiss Axioskop40 polarizing optical microscope equipped with a video camera in crossed polarizer configuration was used. Poly-(tetrafluoroethylene) with a thickness of 25 μm was used as a spacer. The kinetics of superstructure formation was investigated by performing *T*-jumps from high temperatures (above PEG melting) to different final crystallization temperatures where the growth of the axialites was followed. Subsequently, the system was heated with 1 $K\cdot min^{-1}$ and the apparent melting temperature of the superstructure was recorded.

2.6 Differential Scanning Calorimetry (DSC). A Q2000 (TA Instruments) was used for the thermal analysis with respect to the crystallization/melting of PEG and the presence of glass temperatures (T_g). The instrument was calibrated (including baseline calibration) for best performance in the specific temperature range and heating/cooling rate using a sapphire standard. Samples were sealed in an aluminum pan and an empty pan was used as the reference. The temperature protocol involved measurements on heating and subsequent cooling with a rate of 10 K·min^{-1} and in a temperature range between 223 and 423 K.

2.7 Dielectric Spectroscopy. Dielectric Spectroscopy (DS) measurements as a function of temperature (T) were performed with a Novocontrol Alpha frequency analyzer. The temperature protocol involved "isobaric" measurements at atmospheric pressure within the temperature range from 183.15 to 423.15 K in steps of 5 K for frequencies in the range from 10^{-2} to 10^7 Hz. All samples were prepared above the equilibrium melting temperature of PEG and under vacuum by pressing the electrodes to the spacer thickness where necessary. The sample cell consisted of two electrodes, 10 mm in diameter and 50 μm in thickness for all the copolymers, the latter maintained by Teflon spacers. The complex dielectric function, $\varepsilon^* = \varepsilon' - i\varepsilon''$, where ε' is the real and ε'' is the imaginary part, was obtained as a function of angular frequency, ω *(*$= 2\pi f = 1/\tau$*)* and temperature, *i.e.,* $\varepsilon^*(T, \omega)$.[28,29] The analysis was made with the empirical equation of Havriliak and Negami (HN):

$$\varepsilon^*(\omega, T) = \varepsilon_\infty + \sum_k \frac{\Delta\varepsilon_k(T)}{[1 + (i \cdot \omega \cdot \tau_{HN,k}(T))^{m_k}]^{n_k}} + \frac{\sigma_0(T)}{i\varepsilon_0\omega} \qquad (1)$$

where $\Delta\varepsilon_k$ is the dielectric strength, $\tau_{HN,k}$ is the H-N characteristic relaxation time, m_k, n_k (with limits $0.2 < m_k$, $mn_k \leq 1$) describe, respectively, the symmetrical and asymmetrical broadening of the distribution of relaxation times and the index k indicates the process under investigation. At lower frequencies, the dielectric loss sharply rises due to conductivity contribution as $\sigma_0/\varepsilon_0\omega$, where σ_0 is the dc-conductivity and ε_0 (= 8.854×10^{-12} F·m^{-1}) is the permittivity of free space. From $\tau_{HN,k}$, the relaxation times at maximum loss, τ_{max}, were obtained analytically from the HN equation as follows

$$\tau_{max,k} = \tau_{HN,k}[sin\left(\frac{\pi m_k n_k}{2(1+n_k)}\right) / sin\left(\frac{\pi m_k}{2(1+n_k)}\right)]^{1/m_k} \qquad (2)$$

These relaxation times correspond to the relaxation times of the segmental processes. Except for the measured ε'', the derivative of the real part of the dielectric permittivity, ε', ($\mathrm{d}\varepsilon'/\mathrm{dln}\omega \approx (2/\pi)\varepsilon''$) was used in the analysis of the dynamic behavior.

3. RESULTS AND DISCUSSION

The results can be discussed considering two solvent treatment methods and the different molar masses (Table 1). In the first protocol, the aqueous ROPISA polymerization was followed by a freeze drying process (FD), while in the second protocol, a precipitation in organic solvent (OSP) was carried out right after the freeze-drying. Better sample equilibration is achieved with the latter procedure taking into account that this solvent may reduce the influence of the secondary structure coming from the aqueous process. The results are presented in five different sections below: thermodynamic properties, nanophase segregation, secondary structure, superstructure formation and molecular dynamics, each revealing the underlying complexity and multifaceted nature of the PEG-*b*-polypeptide systems. A schematic representation of the lamellar nanodomain morphology found in PEG-*b*-PBLG copolymers is depicted in Scheme 1. Within each block there are multiple levels of organization. In the PEG block, the monoclinic unit cell of PEG, the well-defined crystalline lamellar, and, at much higher length scales, the PEG overarching axialitic superstructures can be identified, while the polypeptide domain embeds the two secondary structures, α- helices and β-sheets, with the former further packed in a hexagonal lattice.

Scheme 1. Schematic representation of the nanodomain morphology of PEG-*b*-PBLG copolymer. The blue color corresponds to the PEG block, while the red color indicates the PBLG block.

3.1 Thermodynamic Properties. With DSC we address the degree of crystallinity, the melting temperatures, the possible liquid-to-glass temperatures and the order-to-disorder transition temperature of the copolymers prepared by FD and OSP protocols. The DSC heating traces are presented in Figure 1, where an endothermic peak appears revealing the melting of PEG crystals. In all copolymers, the melting of the PEG block appears weakly dependent on the peptide block, as it is observed at slightly lower temperatures to that in the respective homopolymer ($T_m^{PEG_{114}} = 333$ K). However, the results differ for the crystallization temperature. Especially in PEG_{114}-*b*-$PBLG_{19}$ copolymer, the PEG compound crystallizes at 278 K (cooling traces shown in Figure S1), with a high

degree of undercooling ($\Delta T \sim 30$ K), in contrast to bulk PEG ($T_c^{PEG_{114}} = 311$ K). The degree of crystallinity in the copolymers can be calculated from the heat of fusion, as $X_c = \frac{1}{w_{PEG}} \frac{\Delta H}{\Delta H_\infty}$, where $\Delta H_\infty = 196\ \mathrm{J \cdot g^{-1}}$.[30] The results are summarized in Table 2, along with the results of WAXS and NMR (to be discussed below).

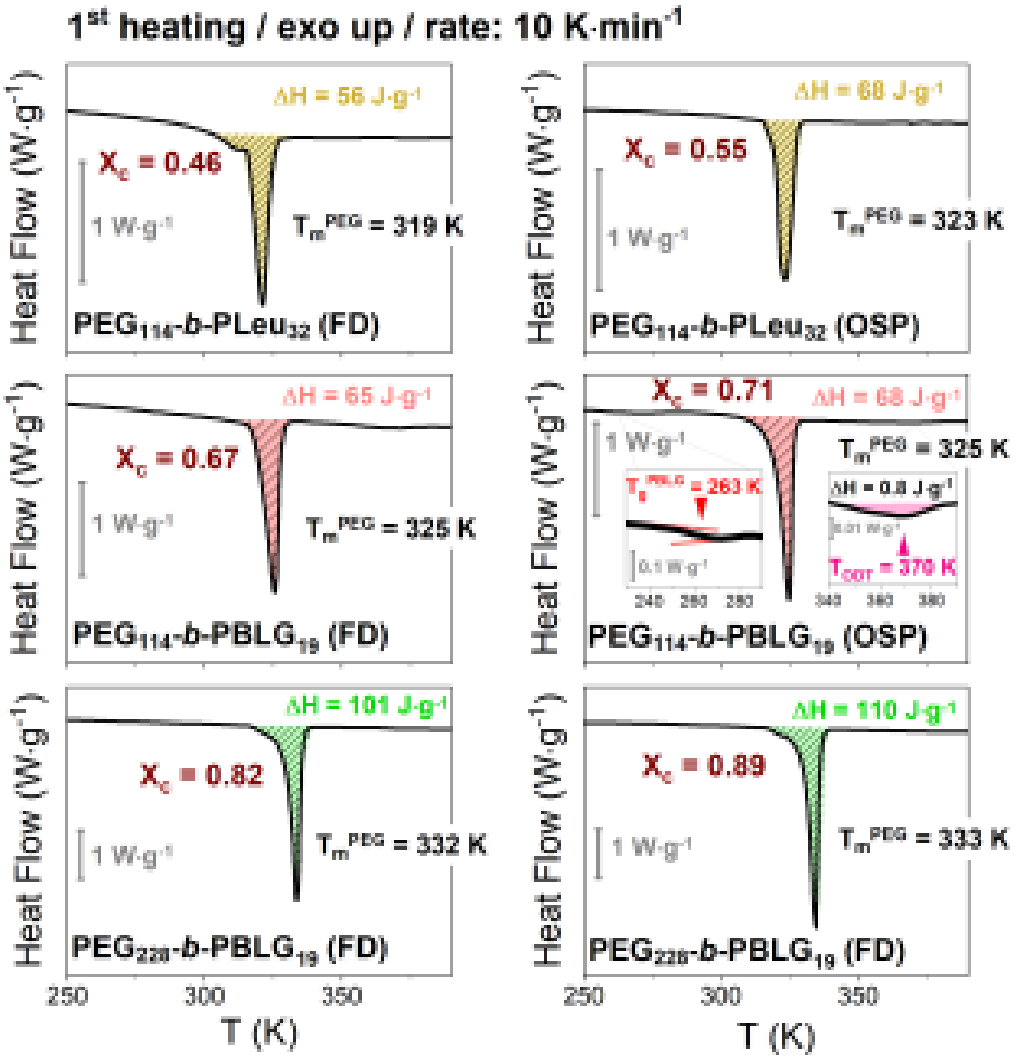

Figure 1. DSC traces of the copolymers, obtained during the first heating at a rate 10 K·min^{-1}. The shadowed areas represent the heat of fusion for the semicrystalline PEG. Melting temperatures $T_m^{PEG_{114}}$ and degrees of crystallinity (X_c) are indicated. For PEG$_{114}$-*b*-PBLG$_{19}$ (OSP) the insets give the glass temperature of the PBLG block (left) and the order-to-disorder transition (with the heat of fusion) of the copolymer (right).

A closer look in the DSC trace of PEG_{114}-*b*-$PBLG_{19}$ (Figure 1 insets or Figure S2) can provide information about additional thermodynamic transitions. At temperature below PEG melting, the glass temperature of the PBLG block is evident (at 263 K), while at temperatures above melting, a first-order transition is indicated, *i.e.* the order-to-disorder transition at T_{ODT} = 370 ± 1 K (value is in agreement with the SAXS results). An estimation of the $(\chi N)_{ODT}$ parameter can be obtained from[31-33] $\Delta H = RT_{ODT} f(1-f)(\chi N)_{ODT}/M_n$, where, ΔH (= 0.8 ± 0.2 J·g^{-1}) is the heat of fusion of the ODT transition, R is the gas constant, f (= 0.52) is the volume fraction of PEG, N (= 133) is the total degree of polymerization, and M_n (= 9160 g·mol^{-1}) is the total molar mass. This estimate provides $(\chi N)_{ODT} = 10 \pm 1$ at the transition, which is in agreement (within the experimental error) with the MFT predictions for diblock copolymers.[34] Overall, the investigation of the thermodynamics revealed an influence of solvent treatment on the PEG degree of crystallinity. Samples prepared by the freeze-drying method display consistently lower degrees of crystallinity. In addition, one of the copolymers prepared by OSP did show an ODT at higher temperatures.

3.2 Nanophase Separation. Precise information about the nanodomain morphology can be obtained by small-angle X-ray scattering. Some representative SAXS curves of PEG_{114}-*b*-$PBLG_{19}$ (OSP) are provided in Figure 2a (as all PEG-*b*-PBLG samples show similar SAXS results). Below the melting temperature of PEG, two Bragg reflections can be identified. The first intense peak, at q_1 = 0.54 nm^{-1} (with periodicity $d_1 = 2\pi/q$ = 11.6 nm), reveals the formation of a lamellar (LAM) structure, indicating nanophase separated PEG/PBLG domains. The second sharper peak, at q_2 = 1.1 nm^{-1} (d_2 = 5.7 nm), reflects the domain spacing of semicrystalline PEG (Figure 2b). At temperatures above PEG melting, the copolymer exhibits a single broad peak, at q_3 ~ 0.6 nm^{-1} (with a periodicity of ~ 10.5 nm), indicative of correlation hole scattering.[35] At T ~ 378 ± 5 K, there is a discontinuous change of the peak intensity, in line with the T_{ODT} obtained by DSC. The SAXS patterns exhibit some additional features at intermediate and higher q with a distinct minimum at $q \sim 2\ nm^{-1}$. They reflect the form factor of PBLG cylinders. In this case, the total scattered intensity is given by the product[36,37]

$$I(q) \sim K \cdot P(q) \cdot S(q) \qquad (3)$$

Where, $P(q)$, is the form factor and, $S(q)$, is the structure factor. The structure factor of the low-q interference peak associated with the inter-sphere correlations can be described by the Percus – Yevick approximation for cylindrical shaped objects, assuming that the interaction between two

"particles" does not depend on particle size or orientation (monodisperse approximation) and is described by a hard-sphere potential as:

$$S(q, R_{\mathrm{h}}, f_{\mathrm{h}}) = \frac{1}{1 + \frac{24 f_{\mathrm{h}} G(A)}{A}} \tag{4}$$

where $A = 2qR_{\mathrm{h}}$, R_{h} and f_{h} are the effective interaction hard-sphere radius and volume fraction parameters describing the interference effects between the PBLG cylinders (*i.e.* the "particles"), and

$$\begin{aligned} G(A) = \frac{\alpha}{A^2}(sinA - AcosA) + \frac{\beta}{A^3}(2AsinA + (2 - A^2)cosA - 2) \\ + \frac{\gamma}{A^5}[-A^4 cosA + 4(3A^2 - 6)cosA + (A^3 - 6A)sinA + 6] \end{aligned} \tag{5}$$

Where,

$$\begin{aligned} \alpha &= (1 + 2f_{\mathrm{h}})^2/(1 - f_{\mathrm{h}})^4 \\ \beta &= -6f_{\mathrm{h}}\,(1 + f_{\mathrm{h}}/2)^2/(1 - f_{\mathrm{h}})^4 \\ \gamma &= {}^1\!/_2\, f_{\mathrm{h}}\,(1 + 2f_{\mathrm{h}})^2/(1 - f_{\mathrm{h}})^4 \end{aligned} \tag{6}$$

The form factor of monodisperse cylinders with a radius R and length L is defined as

$$P(q, R, L) = \int_0^1 \left(2\frac{J_1\left(qR\sqrt{1 - x^2}\right)}{qR\sqrt{1 - x^2}}\frac{\sin(qL\,x/2)}{qL\,x/2}\right)^2 dx \tag{7}$$

where J_1 is the first-order Bessel function. The simulation of the experimental scattering curve using the above theoretical model (Figure 2d) results in a set of four fitting parameters: $R = 2.15 \pm 0.02\ nm, L = 3.0 \pm 0.2\ nm, R_h = 0.87 \pm 0.05\ nm, f_h = 0.48$ (where R_h is the helix radius and L is the helix length). Interestingly, the value of the helix length, L, can be compared with the length of an ideal helix as $\xi_{helix}^{ideal} = 0.15\ nm \cdot 19\ repeat\ units = 2.85\ nm$ (the length of an ideal helix is 0.15 nm per repeat unit).[13,14] This suggests that the persistence length of the helices in the peptide block

increases in the presence of PEG, compared to that of the homopolymer ($\xi_{helix}^{PBLG_{19}} \sim 2\,nm$). At temperatures $T > 378$ K, the broad peak continuously decreases in intensity, signaling the order-to-disorder (ODT) transition (Figure 2c), and the distinct minimum around $q \sim 2\,nm^{-1}$ due to the form factor is lost (Figure 2c). This suggests that mixing of the different blocks eventually destabilizes the PBLG α-helices.

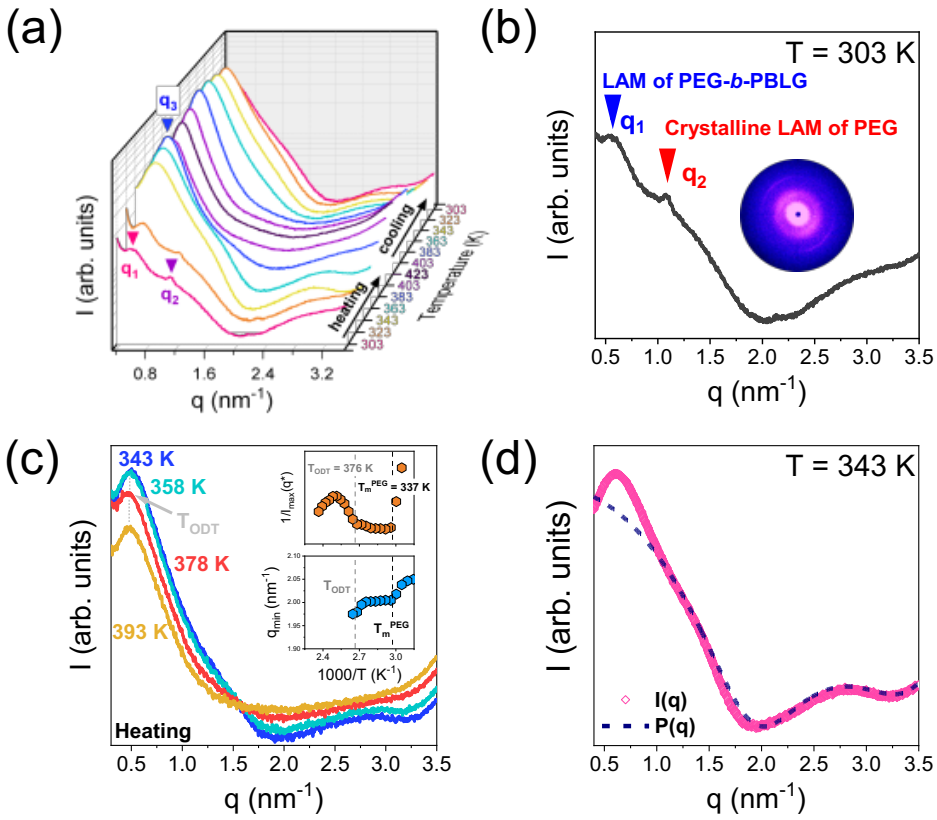

Figure 2. a) SAXS patterns of PEG$_{114}$-*b*-PBLG$_{19}$ (OSP) block copolymer, during heating and subsequent cooling. The vertical arrows give the position of the Bragg reflections corresponding to the lamellar morphology of the copolymer (q_1), the crystalline lamellar of PEG (q_2) and the correlation hole scattering (q_3). b) SAXS pattern of PEG$_{114}$-*b*-PBLG$_{19}$ recorded at 303 K. The corresponding 2D pattern from the extracted fiber is also shown. c) SAXS patterns at 343 K, 358 K, 378 K and 393 K, indicating the characteristic order-to-disorder transition. The insets provide the inverse peak intensity, and the q_{min} (position of the first minima in the form factor) as a function of inverse temperature. The dashed lines indicate the melting and order-to-disorder transition temperatures. d) SAXS pattern of PEG$_{114}$-*b*-PBLG$_{19}$ recorded at 343 K. The blue dashed-line represents the Percus-Yevick approximation for cylindrically shaped objects (eq 7).

The self-assembly in the second diblock system is very different. The SAXS data of PEG$_{114}$-*b*-PLeu$_{32}$ reveal mixing between the two blocks, even at lower temperatures. Within the disordered

state, the structure factor can be described in the context of random phase approximation.[34] The resulting fits are presented in Figure 3a, with the theory effectively describing the experimental data. The extracted interaction parameter displays a weak T dependence as $\chi = 0.07/T + 7 \cdot 10^{-6}$. An estimation of the order-to-disorder temperature can be provided from the representation in Figure 3b. Notice that the T_{ODT} (= 243 K) is significantly below the PEG block crystallization temperature (~ 300 K), indicating that PEG crystallization initiates from the disordered melt state.

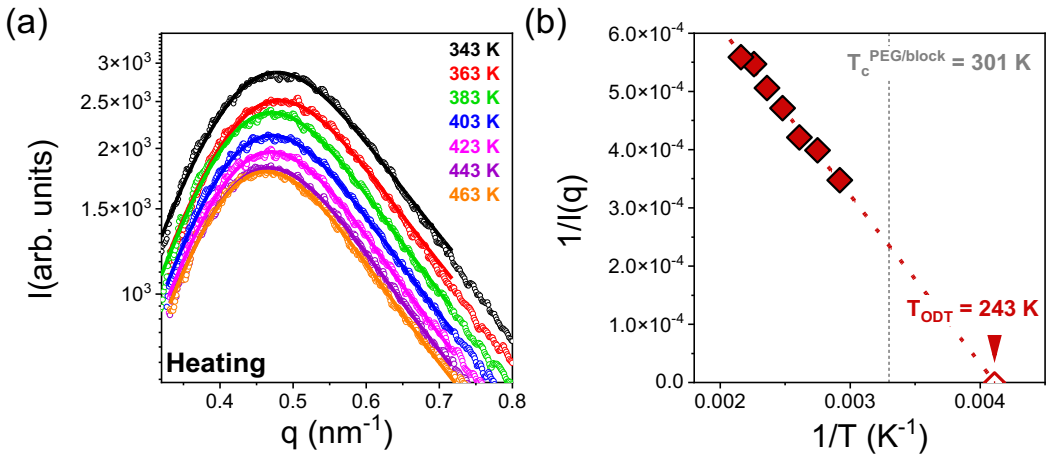

Figure 3. a) SAXS patterns of PEG_{114}-*b*-$PLeu_{32}$ (OSP) at different temperatures, ranging from 343 K to 463 K. A broad scattering maximum is evident, indicating scattering within the disordered state. The solid lines represent fits to the MFT. b) Inverse peak intensity plotted versus inverse temperature. Extrapolating provides an estimate of the hypothetical order-to-disorder transition temperature (243 K). The vertical line gives the crystallization temperature of PEG.

3.3 Secondary Structure. While scattering of X-rays at small angles (SAXS) can identify lower lengthscales, *i.e.* the nanodomain morphology of the copolymer and the crystalline lamellar of PEG, scattering at higher angles (WAXS) can provide the type and the organization of the peptide secondary structure, the PEG unit cell, and an independent measure of the PEG degree of crystallinity.

Figure 4 gives the WAXS patterns of two representative copolymers, PEG_{114}-*b*-$PBLG_{19}$ (FD) and PEG_{114}-*b*-$PLeu_{32}$ (FD), bearing different polypeptide blocks. Figure S3 presents the remaining investigated samples. Starting from intermediate to higher q, both curves display several Bragg reflections – (120), (032), (024), (131) main reflections – corresponding to the ordinary monoclinic unit cell of PEG (unit cell parameters a = 0.81 nm, b = 1.30 nm, c = 1.95 nm and β = 125.4 °),[38] while the amorphous halo reflect the semi-crystalline nature of the copolymers. The degree of crystallinity

of all investigated copolymers can be calculated as $X_c^{XRD} = \frac{1}{f_{PEG}} \frac{I_c}{I_a + I_c}$, where f_{PEG} is the volume fraction of PEG (Table 1), I_c is the intensity of all Bragg reflections associated with the monoclinic unit cell and I_a is the intensity of the amorphous halo (results from different methods are summarized in Table 2). The results show higher crystallinity in the OSP samples, compared to the FD samples. This effect can be attributed to the synthesis protocol of the copolymers.

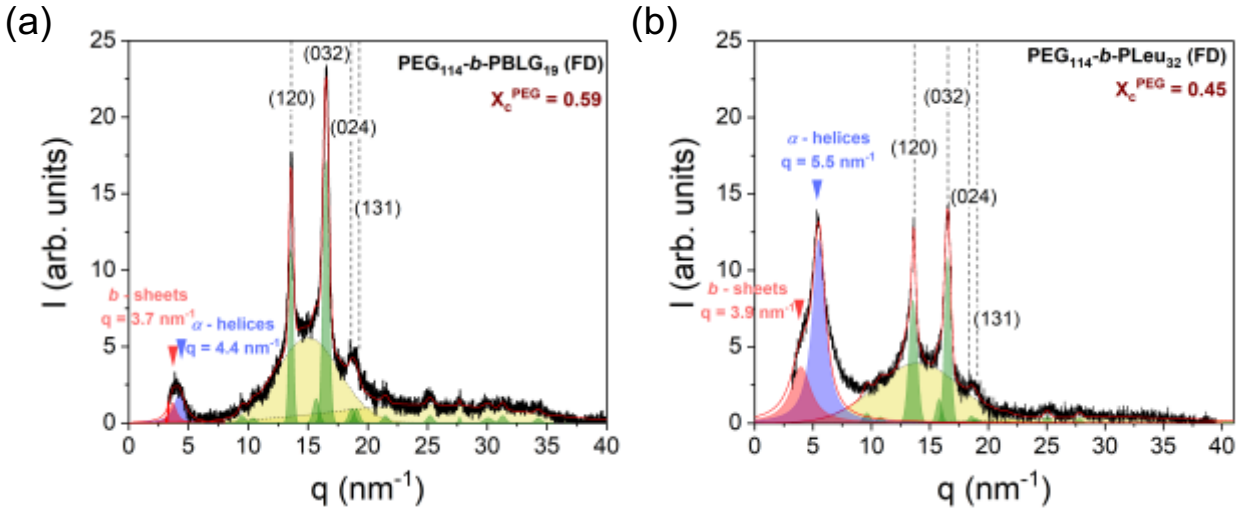

Figure 4. WAXS patterns of (a) PEG_{114}-*b*-$PBLG_{19}$ (FD) and (b) PEG_{114}-*b*-$PLeu_{32}$ (FD). At lower *q*, red arrows indicate the lamellar spacing of *b*-sheet secondary structure, while blue arrows give the position of the primary reflection from the weakly hexagonally packed cylinders composed from *α*-helical PBLG segments. At higher *q*, the short-dashed lines indicate the (*hkl*) indices of the Bragg reflections corresponding to the monoclinic unit cell of PEG, whereas the yellow areas give the contribution from the amorphous part.

Table 2. PEG degree of crystallinity as calculated from WAXS, ^{13}C NMR and DSC.

Samples	X_c^{WAXS}	X_c^{NMR}	X_c^{DSC}
PEG_{114}-*b*-$PLeu_{32}$ (FD)	0.45	0.27	0.46
PEG_{114}-*b*-$PLeu_{32}$ (OSP)	0.51	0.49	0.55
PEG_{114}-*b*-$PBLG_{19}$ (FD)	0.59	0.57	0.67
PEG_{114}-*b*-$PBLG_{19}$ (OSP)	0.67	0.66	0.71
PEG_{228}-*b*-$PBLG_{19}$ (FD)	0.68	0.69	0.82
PEG_{228}-*b*-$PBLG_{19}$ (OSP)	0.78	0.80	0.89

At lower q (q < 10 nm^{-1}), both copolymers reveal features associated with the peptide secondary structure. Literature data from well-oriented PBLG[13,14] reveal an α-helical secondary structure conformation with residues on a spiral pitch of 0.54 nm in a 18/5 helix (18 residues in 5 turns) with a repeat unit of c = 2.7 nm. The structure was ascribed to the paracrystalline form C; it consists of a periodic packing of α-helices in the direction lateral to the chain axis with a nematic-like paracrystalline order. The first strong equatorial reflection of PBLG at q = 4.4 nm^{-1} corresponds to the (10) reflection from a hexagonal unit cell of PBLG helices with a unit cell parameter of a = 1.65 nm. In the present copolymer PEG$_{114}$-*b*-PBLG$_{19}$ (Figure 4a), α-helices exist in the absence of long range order as revealed by the absence of higher order peaks. In addition, because of the low molar mass of PBLG, the presence of β-sheets at q ~ 3.7 nm^{-1} is also evident.[13] Respectively, for PEG$_{114}$-*b*-PLeu$_{32}$ (Figure 4b), the primary peak at q ~ 5.5 nm^{-1} for the PLeu peptide block indicates the presence of weakly hexagonally packed α-helices (intercylinder distance of ~ 1.32 nm), while β-sheets are shown from the weak Bragg peak at q ~ 3.9 nm^{-1}.[39]

As a next step, we investigate the effect of thermal annealing in Figure 5. Each secondary structure can be identified, as noted above, from its characteristic Bragg reflection, with the intensity of the peak corresponding to the relative β-sheet/α-helical fraction (in calculating fractions from WAXS assume only ordered secondary structures such α-helices and β-sheets) in the peptide block (as shown in Table 3). Both before and after annealing, α-helices are the dominant secondary structure in all copolymers. As anticipated, the OSP samples exhibit higher relative α-helical fractions, as the helices are the most stable secondary structure the peptide can form at equilibrium.

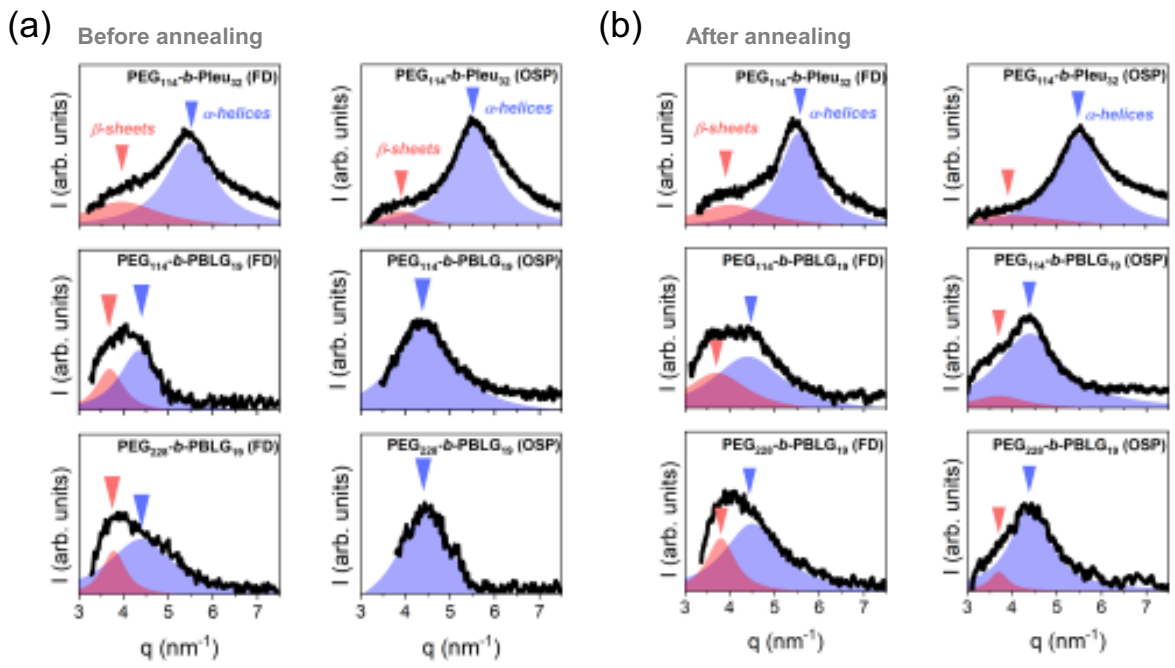

Figure 5. WAXS patterns of the copolymers (a) before and (b) after annealing for 1 day at 343 K. Red arrows identify the characteristic distance of *β*-sheets, while blue arrows indicate the position of the primary reflection associated with the *α*-helices.

Table 3. Relative fractions of *α*-helices and *β*-sheets in the peptide blocks of the investigated copolymers, as calculated from WAXS (before and after annealing) and absolute fractions of *α*-helices, *β*-sheets and random coil, as calculated from NMR (at 298 K and 343 K).

Samples	WAXS				NMR					
	β-sheets		*α*-helices		*β*-sheets		*α*-helices		random coil	
	b.a.*	a.a.*	b.a.*	a.a.*	298 K	343 K	298 K	343 K	298 K	343 K
PEG_{114}-*b*-$PLeu_{32}$ (FD)	0.33	0.34	0.67	0.66	0.35	0.38	0.45	0.41	0.20	0.21
PEG_{114}-*b*-$PLeu_{32}$ (OSP)	0.14	0.24	0.86	0.76	0.20	0.19	0.67	0.69	0.13	0.12
PEG_{114}-*b*-$PBLG_{19}$ (FD)	0.33	0.38	0.67	0.62	0.20	0.31	0.72	0.56	0.08	0.13
PEG_{114}-*b*-$PBLG_{19}$ (OSP)	0	0.13	1	0.87	0.02	0.13	0.93	0.73	0.05	0.14
PEG_{228}-*b*-$PBLG_{19}$ (FD)	0.22	0.31	0.78	0.69	0.19	0.32	0.81	0.57	-	0.11
PEG_{228}-*b*-$PBLG_{19}$ (OSP)	0	0.17	1	0.87	0.04	0.16	0.96	0.75	-	0.09

*b.a. = before annealing, a.a. = after annealing

One of the key probes for peptide secondary structure determination and PEG crystallinity determination is Solid State ^{13}C NMR.[40-42] The characteristic traces of the investigated copolymers are shown in Figure 6a at 298 K and in Figure 6b at 343 K. Starting from the PEG blocks, the intense resonances at $\delta \sim 73$ ppm and ~ 71 ppm are assigned to the crystalline and amorphous signals,

respectively.[43] On the other hand, the resonances at $\delta \sim 176$ ppm (~ 172 ppm) and $\delta \sim 58$ ppm (~ 53 ppm), arising from the chemical shifts of the amide C=O and C_α carbon, respectively, reveal the formation of an α-helical (β-sheet) secondary structure in the peptide blocks. A distinct advantage of Solid State ^{13}C NMR is the additional identification of the random coil conformations, which can be detected from the resonances at $\delta \sim 53$ ppm of the C_α carbon. A quantitative analysis of the intensity of the resonances can determine the degree of crystallinity (Table 2) and the α-helical/β-sheet fractions (Table 3) in the copolymers.

In addition to the peptide secondary structure, ^{13}C NMR provides the PEG crystallinity. Overall, the degree of crystallinity calculated from NMR show excellent agreement with the WAXS results (Table 2). Potential discrepancies in the values, *i.e.* in the case of PEG_{114}-*b*-$PLeu_{32}$ (FD), arise from the restricted amorphous fractions in the PEG block and the size of its crystals. Concerning the secondary structure fractions, the comparison between the NMR results at 298 (343) K and the WAXS results before (after) annealing highlights the difference between the two probes. The ability to access the random coil fraction (*absolute fractions*) is now expressed as a "loss" in the α-helical content (Table 3). This underscores the complementary nature of NMR and WAXS results, in providing a comprehensive understanding (from the different chemical shifts) of the amorphous and crystalline PEG and the peptide secondary structure. The secondary structure investigation by a combination of WAXS and solid state NMR revealed a higher α-helical content in the copolymers following the slow precipitation in organic solvent as opposed to the freeze drying process, at the expense of the content of β-sheets and random coils. Furthermore PEG-*b*-PLeu contains a high fraction of β-sheets when prepared via freeze drying.

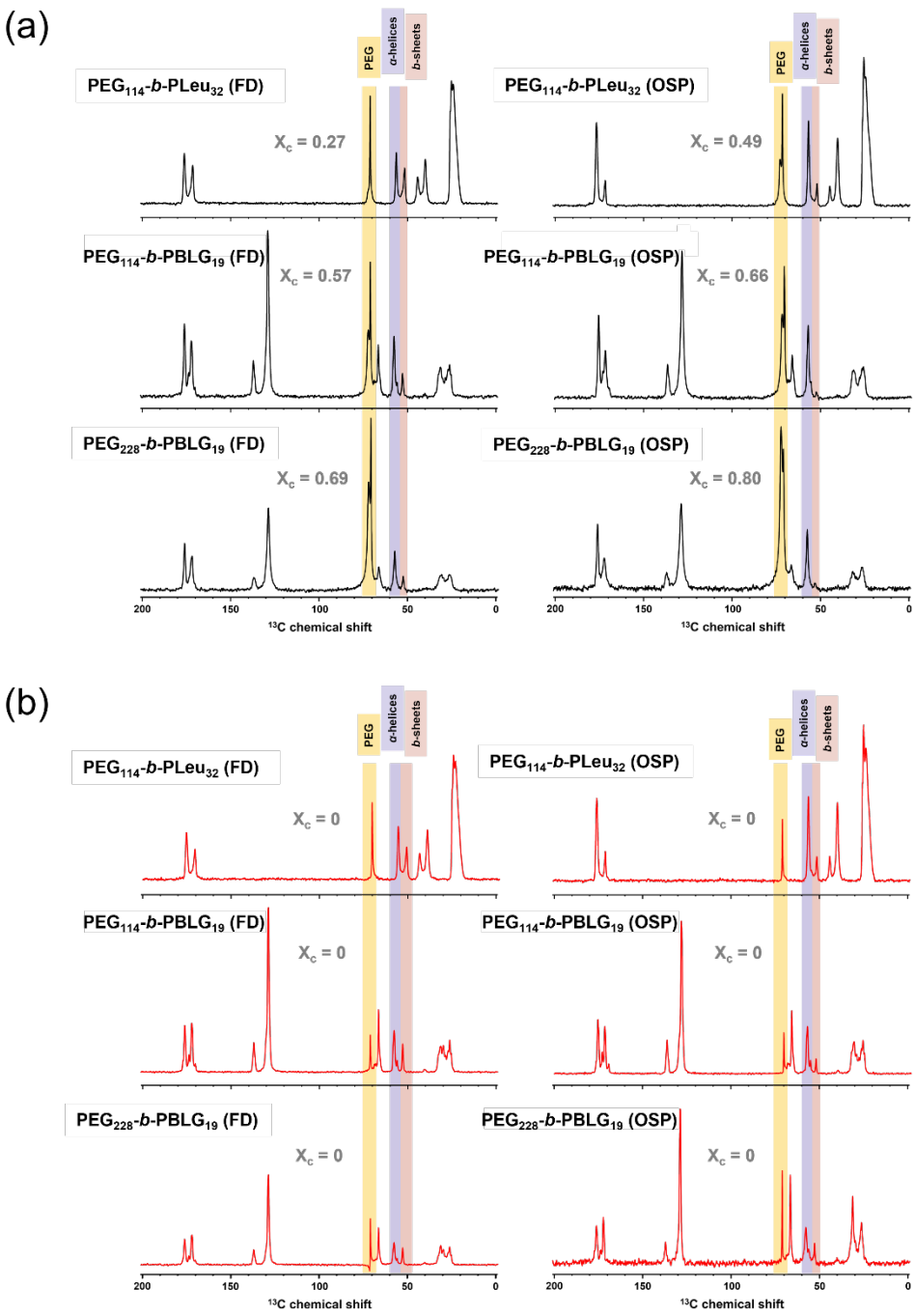

Figure 6. ^{13}C solid state NMR traces of the investigated copolymers at (a) 298 K and (b) 343 K. The highlighted areas refer to the chemical shifts used for the calculations of the degree of crystallinity (PEG) and the fraction of peptide (PBLG, PLeu) secondary structure (see text).

3.4 Superstructure Identification. The organization at a much higher lengthscale (superstructure) was studied by POM. Some representative POM images of PEG_{114}-*b*-$PBLG_{19}$ are

shown in Figure 7. Interestingly, the superstructures deviate from the usual spherulitic-shape of PEG bulk. The copolymer forms an axialitic crystalline morphology, demonstrating a distorted Maltese cross pattern.

Figure 7. Representative POM images of the axialitic superstructures of PEG_{114}-*b*-$PBLG_{19}$ under isothermal conditions at $T = 286$ K.

Subsequently, the kinetics of the superstructure formation were investigated (Figure 8) and the different growth rates were obtained under isothermal conditions for different crystallization temperatures. Differences can be seen in both the temperature and the size of the axialites observed, in comparison to the spherulites found in the bulk PEG. The effect of thermodynamic confinement due to the presence of the PBLG block is threefold: First, the copolymers crystallize at lower temperatures (DSC results). Second, the inherent shape anisotropy of the PEG superstructures grows with time (Figure 8a). Third, the growth rates of the axialites, when examined at a fixed temperature, are about 7 orders of magnitude slower than those of the PEG homopolymer (Figure 8b). Additionally, as presented in Figure 8d, the PEG crystals in the copolymers exhibit lower equilibrium melting temperatures, in comparison to PEG_{114}, suggesting thermodynamic confinement and mixing. Concerning the PEG_{114}-*b*-$PLeu_{32}$ copolymer, formation of some axialitic superstructures was also observed but the analysis of the growth rates was prohibited due to the extensive mixing between the two blocks (Figure 3).

Figure 8. (a) Length of the long (filled symbols) and short (open symbols) axes (radius) of the PEG axialites (spherulites) as a function of time for PEG_{114}-*b*-$PBLG_{19}$ copolymers (bulk PEG_{114}). (b) Growth rates of the superstructures as a function of the inverse crystallization temperature. Green and blue symbols correspond to FD and OSP PEG_{114}-*b*-$PBLG_{19}$ copolymers; dark and light colors represent the long and short axes, respectively. Red symbols represent the bulk PEG. Arrows indicate the equilibrium melting temperature and the glass temperatures for the PEG and PBLG block in the OSP prepared copolymer. (c) POM image, obtained under isothermal conditions for bulk PEG_{114} at 311 K and the PEG_{114}-*b*-$PBLG_{19}$ copolymer at 286 K. (d) Apparent melting temperatures plotted against the crystallization temperature. Green and blue correspond to the PEG_{114}-*b*-$PBLG_{19}$ (FD), and PEG_{114}-*b*-$PBLG_{19}$ (OSP) copolymers, respectively, while red represents the bulk PEG. The slope (dashed lines) of the two copolymers were held constant (from the bulk PEG). Star symbols indicate the extrapolated equilibrium melting temperatures.

3.5 Multiple Levels of Organization. The structured results can be summarized in a graphic plot, (Figure 9), depicting the investigated lengthscales and the corresponding probes employed. Firstly, NMR identified the peptide secondary structures (α-helices, β-sheets as well as some random coil configurations). Secondly, WAXS provided the unit cell of the semicrystalline PEG block. Third, SAXS measurements revealed three ordered "objects": the form factor of PBLG α-helices, the domain spacing of the semicrystalline PEG, and the (lamellar) nanodomain morphology of the copolymer. Earlier TEM and AFM results provided some rod-like intermediate structures. At even longer lengthscales, POM documented the formation of axialitic superstructures. It was further shown that the growth of the latter superstructures was depended on the solvent treatment protocol. Overall, there exist six levels of organization in copolymers prepared by the ROPISA method imitating the multiple levels of organization found in natural materials.

Figure 9. Schematic representation of the different lengthscales investigated for the PEG-*b*-PBLG copolymer. Starting from lower lengthscales, the secondary structures (α-helices and β-sheets), the PEG unit cell, the nanodomain morphology, an intermediate rod-like structure and the axialitic superstructure can be identified, using a combination of probes (NMR, WAXS, SAXS, TEM/AFM and POM).

3.6 Molecular Dynamics. A comprehensive understanding of the copolymers requires both static and dynamic probes. While the static probes provided insights on the self-assembly of the copolymers over the several lengthscales, it is the molecular dynamic that can reveal the local and global peptide dynamics. Earlier combined studies by dielectric spectroscopy solid state NMR on PBLG as a function of molar mass revealed very rich dynamic behavior.[14] They have shown that the origin of the liquid-to-glass temperature observed in DSC was related to the low persistence length of the α-helical secondary structures. A broken network of hydrogen bonds responsible for the dynamic arrest at the glass temperature was also responsible for the low persistence of the helical segments. These processes were very distinct in dielectric spectroscopy. A fast segmental process with a strong temperature dependence (according to the Vogel-Fulcher-Tammann -VFT- equation) was followed by a slower process associated with the relaxation of helical parts. The dielectric strength of the slower process was employed in calculating the persistence length of the helices.[13,14]

The corresponding DS results for the PEG_{114}-*b*-$PBLG_{19}$ (OSP) can be discussed with the help of Figure 10. For clarity, the processes below glass temperature of PEG have been omitted. Two

segmental processes can be identified at T > T_g^{PEG}. The faster one corresponds to the segmental dynamics of the PEG block, while the slower one is ascribed to the segmental relaxation of the PBLG block. The two processes approach each other in the copolymer, revealing some degree of molecular mixing at the interface between the blocks. At temperatures above 293 K, the motion of the ions trapped in the crystalline PEG block is also evident for both PEG_{114}-*b*-$PBLG_{19}$ (OSP) and PEG_{114}-*b*-$PBLG_{19}$ (FD). It can be seen that ions move faster in the latter case. This can be explained through two competing factors in the PEG_{114}-*b*-$PBLG_{19}$ (FD): the mixing of the PEG block with the slower PBLG block, which decreases ion mobility, versus the reduced crystallinity of PEG, that increases ion mobility. The experimental data suggest the predominance of the second factor. At higher temperatures, electrode polarization and Maxwell-Wagner-Sillars interfacial polarization mask any molecular processes (such the one associated with the relaxation of PBLG α-helices). Nevertheless, the DS results revealed two segmental processes in the PEG_{114}-*b*-$PBLG_{19}$ copolymers and molecular mixing at the interface.

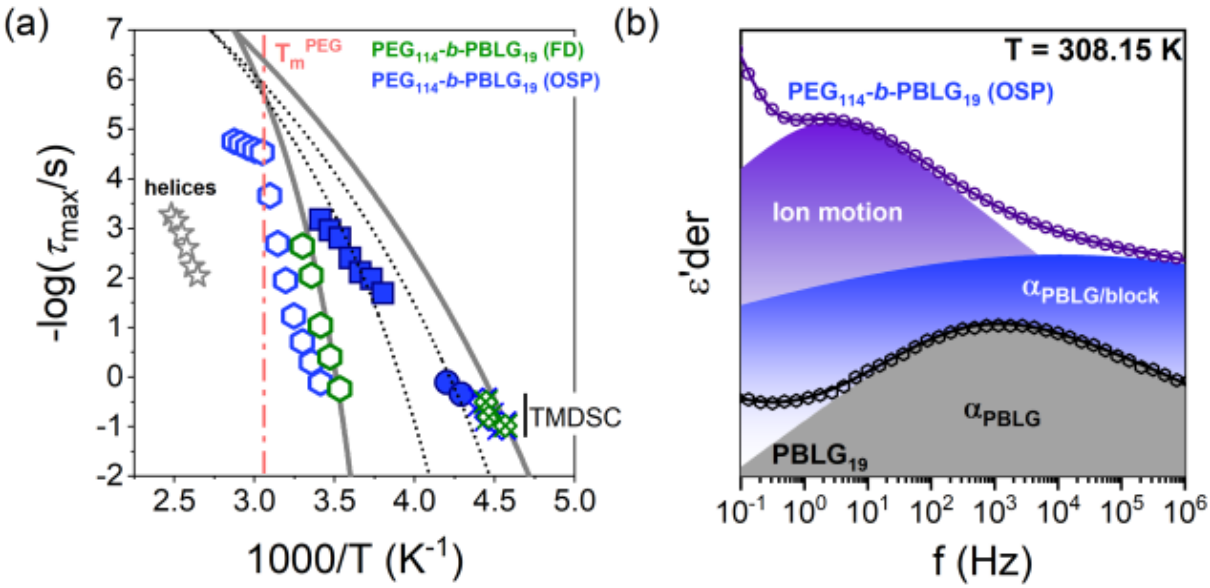

Figure 10. (a) Relaxation times as a function of the inverse temperature for the different processes of PEG_{114}-*b*-$PBLG_{19}$ (OSP) (blue) and PEG_{114}-*b*-$PBLG_{19}$ (FD) (green). Circles represent the segmental process of PEG, squares the segmental process of PBLG and hexagons the motion of ions. Doted black lines represent indicative fits to the PEG and PBLG segmental processes. Pink line indicates the melting temperature of the PEG block. Solid gray lines are simulation of the VFT function for the bulk PEG and PBLG homopolymers (Table S1), while gray stars represent the slow helix process in bulk PBLG. TM-DSC data are also presented with crosses. (b) Derivative of dielectric permittivity as a function of frequency for PEG_{114}-*b*-$PBLG_{19}$ (OSP) (circles), and bulk $PBLG_{19}$ (hexagons). Blue and purple areas of the copolymer correspond to simulations of the

segmental process and the ion motion, respectively. The grey area represents the α process in the $PBLG_{19}$ homopolymer.

4. CONCLUSION

Ring-opening polymerization-induced self-assembly in aqueous buffer using γ-benzyl-L-glutamate N-carboxyanhydrides in the presence of α-amino-poly(ethylene glycol) initiators controls unwanted water-induced NCA ring-opening (by the formation of protective micelles) and gives rise to amphiphilic block copolymers with several levels of organization. Six levels of organization were found in the PEG-*b*-PBLG copolymers imitating the multiple levels of organization found in natural materials. They comprise: the lamellar nanodomain morphology of unlike blocks, the domain spacing of semicrystalline PEG within its monoclinic unit cell, the peptide secondary structures (α-helices and β-sheets) within the PBLG nanodomain, and at longer lengthscales some rod-like structures (typically ~ 100 nm in size) and the strongly asymmetric superstructures of PEG crystals (typically ~ 100 μm in size).

Furthermore, the type of NCA monomer (BLG-NCA vs Leu-NCA) had an influence on the degree of segregation and the order-to-disorder transition temperature in the PEG-*b*-PBLG and PEG-*b*-PLeu copolymers. The latter have shown mixing of the unlike blocks at a temperature above the melting of PEG. In contrast, the low-q scattering of PEG-*b*-PBLG revealed a lamellar nanodomain morphology that could be described by the Percus-Yevick approximation for cylindrical shaped

objects with a helix length approaching an "ideal" helix. At temperatures above the ODT, mixing of the unlike blocks resulted in the destabilization of the PBLG α-helices.

REFERENCES

1. Perly, B.; Douy, A.; Gallot, B. Block Copolymers Polybutadiene/Poly(benzyl-L-glutamate) and Polybutadiene/Poly(N^5-hydroxypropylglutamine) Preparation and Structural Study by X-Ray and Electron Microscopy. *Makromol. Chem.* **1976**, *177*, 2569-2589.
2. Douy, A.; Gallot, B. Block Copolymers with a Polyvinyl and a Polypeptide Block: Factors Governing the Folding of the Polypeptide Chains. *Polymer* **1982**, *23*, 1039.
3. Klok, H. A.; Langenwalter, J. F.; Lecommandoux, S. Self-Assembly of Peptide-Based Diblock Oligomers. *Macromolecules.* **2000**, *33*, 7819-7826.
4. Lecommandoux, S.; Achard, M.-F.; Langenwalter, J.F.; Klok, H.-A. Self-Assembly of Rod-Coil Diblock Oligomers Based on α-Helical Peptides. *Macromolecules* **2001**, *34*, 9100-9111.
5. Schlaad, H.; Kukula, H.; Smarsly, B.; Antonietti, M.; Pakula, T. Solid-State Morphologies of Linear and Bottlebrush-Shaped Polystyrene-Poly(Z-L-lysine) Block Copolymers. *Polymer* **2002**, 43, 5321-5328.
6. Floudas, G.; Papadopoulos, P.; Klok, H.A.; Vandermeulen, G.W.M.; Rodriguez-Hernandez, J. Hierarchical Self-Assembly of Poly(γ-benzyl-L-glutamate)-Poly(ethylene glycol)-Poly(γ-benzyl-L-glutamate) Rod-Coil-Rod Triblock Copolymers. *Macromolecules* **2003**, *36*, 3676-3683.
7. Schlaad, H.; Smarsly, B.; Losik, M. The Role of Chain-Length Distribution in the Formation of Solid-State Structures of Polypeptide-Based Rod-Coil Block Copolymers. *Macromolecules* **2004**, *37*, 2210-2214.
8. Tanaka, S.; Ogura, A.; Kaneko, T.; Murata, Y.; Akashi, M. Precise Synthesis of ABA Triblock Copolymers Comprised of Poly(ethylene oxide) and Poly(β-benzyl-L-aspartate): A Hierarchical Structure Inducing Excellent Elasticity. *Macromolecules* **2004**, *37*, 1370-1377.
9. Klok, H. A.; Lecommandoux, S. Solid-State Structure, Organization and Properties of Peptide-Synthetic Hybrid Block Copolymers. *Adv. Polym. Sci.* **2006**, *202*, 75-111.
10. Block, H. *Poly(γ-benzyl-L-glutamate) and Other Glutamic Acid Containing Polymers.* Gordon and Breach Science Publishers, **1983**, New York, NY 10016.
11. Muroga, Y.; Nagasawa, M. On the Flexibility of Poly(γ-Benzyl L-Glutamate) in Helicogenic Solvents. *Biopolymers* **1998**, *45*, 281–288.
12. Schlaad, H. Solution Properties of Polypeptide-based Copolymers. *Adv. Polym. Sci.* **2006**, *202*, 53-73.

13. Papadopoulos, P.; Floudas, G.; Klok, H.-A.; Schnell, I.; Pakula, T. Self-Assembly and Dynamics of Poly(γ-benzyl-L-glutamate) Peptides. *Biomacromolecules* **2004**, *5*, 81.
14. Floudas, G.; Spiess, H.W. Self-Assembly and Dynamics of Polypeptides. *Macromol. Rapid Commum.* **2009**, *30*, 278-298.
15. Duncan, R. The dawning era of polymer therapeutics. *Nature Reviews Drug Discovery* **2003**, 2, 347–360.
16. Kugo, K.; Ohji, A.; Uno, T.; Nishino, J. Synthesis and Conformations of A-B-A Tri-Block Copolymers with Hydrophobic Poly(γ-benzyl-L-glutamate) and Hydrophilic Poly(ethylene oxide). *Polymer Journal* **1987**, 19, 375–381.
17. Cho, C.-S.; Kim, S.-W.; Komoto, T. Synthesis and structural study of an ABA block copolymer consisting of poly(γ-benzyl-L-glutamate) as the A block and poly(ethylene oxide) as the B block. *Die Makromolekulare Chemie* **1990**, 191, 981–991.
18. Cho, C.-S.; Nah, J.-W.; Jeong, Y.-I.; Cheon, J.-B.; Asayama, S.; Ise, H.; Akaike, T; Conformational transition of nanoparticles composed of poly(γ-benzyl-L-glutamate) as the core and poly(ethylene oxide) as the shell. *Polymer* **1999**, 40, 6769–6775.
19. Parras, P.; Castelletto, V.; Hamley, I. W.; Klok, H.-A. Nanostructure formation in poly(γ-benzyl-L-glutamate)–poly(ethylene glycol)–poly(γ-benzyl-L-glutamate) triblock copolymers in the solid state. *Soft Matter* **2005**, 1, 284.
20. d'Agosto, F.; Rieger, J.; Lansalot, M. RAFT-mediated polymerization-induced self-assembly. *Angewandte Chemie International Edition* **2020**, 59, 8368–8392.
21. Penfold, N. J. W.; Yeow, J.; Boyer, C.; Armes, S. P. Emerging Trends in Polymerization-Induced Self-Assembly. *ACS Macro Letters* **2019**, 8, 1029–1054.
22. Grazon, C.; Salas-Ambrosio, P.; Ibarboure, E.; Buol, A.; Garanger, E.; Grinstaff, M. W.; Lecommandoux, S.; Bonduelle, C. Aqueous Ring-Opening Polymerization-Induced Self-Assembly (ROPISA) of N-carboxyanhydrides. *Angew. Chem. Int. Ed.* **2019**, 59, 622 –626.
23. Grazon, C.; Salas-Ambrosio, P.; Antoine, S.; Ibarboure, E.; Sandre, O.; Clulow, A. J.; Boyd, B. J.; Grinstaff, M. W.; Lecommandoux, S.; Bonduelle, C. Aqueous ROPISA of α-Amino Acid N-Carboxyanhydrides: Polypeptide Block Secondary Structure Controls Nanoparticle Shape Anisotropy. *Polym. Chem.* **2021**, 12, 6242–6251.
24. Meyers, M.A.; Chen, P.Y.; Lin, A.Y.M.; Seki, Y. Biological materials: Structure and mechanical properties. *Progress in materials science* **2008**, 53, 1–206.

25. Fetters, L.J.; Lohse, D.J.; Richter, D.; Witten, T.A.; Zirkel, A. Connection between polymer molecular weight, density, chain dimensions, and melt viscoelastic properties. *Macromolecules* **1994**, 27, 4639–4647.
26. Papadopoulos, P.; Floudas, G.; Schnell, I.; Aliferis, T.; Iatrou, H.; Hadjichristidis, N. Nanodomain-Induced Chain Folding in Poly(*γ*-benzyl-L-glutamate)-*b*-polyglycine Diblock Copolymers. *Biomacromolecules* **2005**, 6, 2352–2361.
27. Poly-L-leucine, Chemsrc.com. Available at: https://www.chemsrc.com/en/cas/25322-63-8_1375819.html.
28. Kremer, F. and Schönhals, A. in *Broadband Dielectric Spectroscopy*, Springer, Berlin, (**2002**).
29. Floudas, G.; Paluch, M.; Grzybowski, A.; Ngai, K. L. in *Molecular Dynamics of Glass-Forming Systems. Effects of Pressure*, Springer-Verlag Berlin Heidelberg (**2011**).
30. Zardalidis, G.; Mars, J.; Allgaier, J.; Mezger, M.; Richter, D.; Floudas, G. Influence of chain topology on polymer crystallization: poly(ethylene oxide) (PEO) rings vs. linear chains. *Soft Matter* **2016**, 12, 8124–8134.
31. Kasten, H.; Stühn, B. Density discontinuity at the microphase separation transition of a symmetric diblock copolymer. *Macromolecules* **1995**, 28, 4777–4778.
32. Hajduk, D.A.; Gruner, S.M.; Erramilli, S.; Register, R.A; Fetters, L.J. High-Pressure Effects on the Order− Disorder Transition in Block Copolymer Melts. *Macromolecules* **1996**, 29, 1473–1481.
33. Floudas, G.; Vazaiou, B.; Schipper, F.; Ulrich, R.; Wiesner, U.; Iatrou, H.; Hadjichristidis, N. Poly (ethylene oxide-b-isoprene) diblock copolymer phase diagram. *Macromolecules* **2001**, 34, 2947–2957.
34. Leibler, L. *Theory of Microphase Separation in Block Copolymers*. Macromolecules **1980**, 13, 1602–1617.
35. De Gennes, P.G. in *Scaling Concepts in Polymer Physics*. Cornell University Press (**1979**)
36. Kinning, D. J.; Thomas, E. L. Hard-Sphere Interactions between Spherical Domains in Diblock Copolymers. *Macromolecules* **1984**, 17, 1712-1718.
37. Pedersen, J. S. Determination of Size Distributions from Small-Angle Scattering Data for Systems with Effective Hard-Sphere Interactions. *J. Appl. Cryst.* **1994**, 27, 595-608.
38. Takahashi, Y.; Tadokoro, H. Structural Studies of Polyethers, (–(CH2)m–O–)n. X. Crystal Structure of Poly(ethyleneoxide). *Macromolecules* **1973**, 6, 672-675.

39. Mondeshki, M.; Spiess, H. W.; Aliferis, T.; Iatrou, H.; Hadjichristidis, N.; Floudas, G. Hierarchical self-assembly in diblock copolypeptides of poly(*γ*-benzyl-L-glutamate) with poly poly(L-leucine) and poly(O-benzyl-L-tyrosine). *European Polymer Journal* **2011**, 47, 668–674.
40. Shoji, A.; Ozaki, T.; Saito, H.; Tabeta, R.; Ando, I. Conformational Characterization of Solid Polypeptides by ^{13}C NMR Recorded by the Cross Polarization-Magic Angle Spinning Method: Conformation-Dependent ^{13}C Chemical Shifts of Oligo- and Poly(γ-benzyl L-glutamates) and Sequential Copolymers of γ-Benzyl and γ-Methyl L-Glutamates and Qualitative Evaluation of Side-Chain Orientation. *Macromolecules* **1984**, 17, 1472.
41. van Beek, J.D.; Beaulieu, L.; Schafer, H.; Demura, M.; Asakura, T.; Meier, B.H. Solid-state NMR determination of the secondary structure of Samia cynthia ricini silk. *Nature* **2000**, 405, 1077.
42. Tycko, R. Biomolecular Solid State NMR: Advances in Structural Methodology and Applications to Peptide and Protein Fibrils. *Ann. Rev. Phys. Chem.* **2001**, 52, 575.
43. Wang, S.; Kang, J.; Jain, D.; Miyoshi, T. *Application of NMR in polymer characterization*. In Nuclear Magnetic Resonance; The Royel Society of Chemistry: Cambridge, UK (**2016**), 45, 79–82.

SUPPORTING INFORMATION

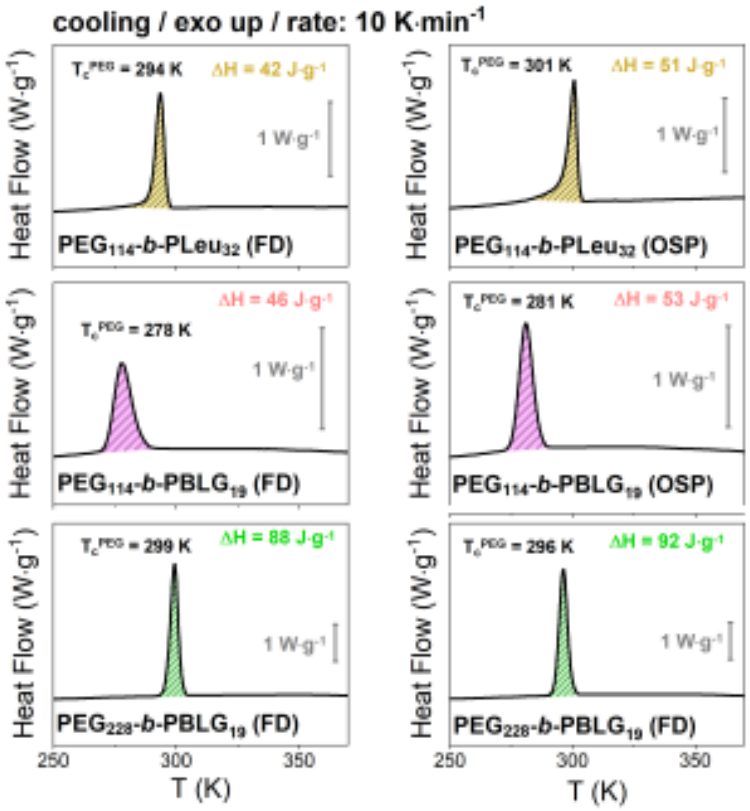

Figure S1. DSC traces of the copolymers, obtained during the cooling at a rate 10 K·min^{-1}. The shadowed areas represent the heat of fusion for the semicrystalline PEG for each sample. Crystallization temperatures are also indicated.

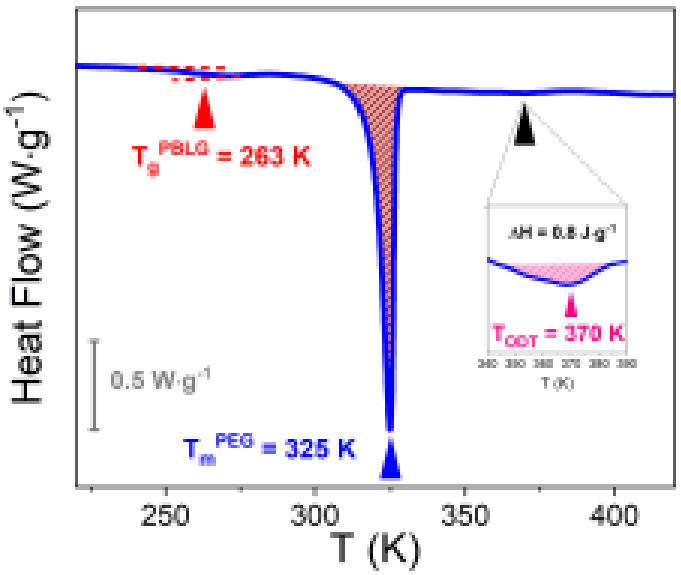

Figure S2. DSC trace of the PEG_{114}-*b*-$PBLG_{19}$ (OSP) copolymer, obtained during the heating at a rate 10 $K \cdot min^{-1}$. The shadowed areas represent the heat of fusion for the semicrystalline PEG and the ODT transition. Starting from lower temperatures: blue arrow represents the glass temperature of the PBLG block, purple arrow represents the melting temperature of the PEG block and pink arrow indicates the ODT transition temperature.

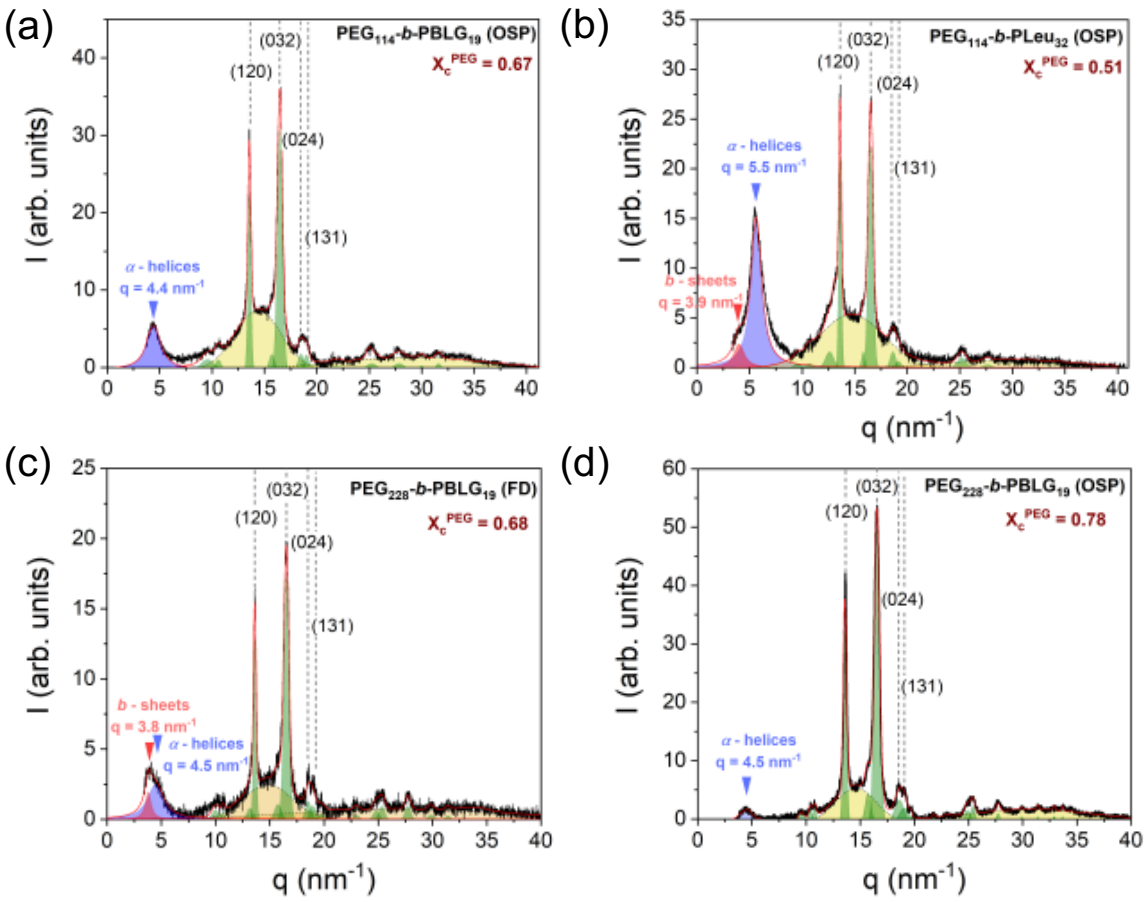

Figure S3. WAXS patterns of (a) PEG$_{114}$-*b*-PBLG$_{19}$ (OSP), (b) PEG$_{114}$-*b*-PLeu$_{32}$ (OSP), (c) PEG$_{228}$-*b*-PBLG$_{19}$ (FD) and (d) PEG$_{228}$-*b*-PBLG$_{19}$ (OSP).

Table 1. Vogel – Fulcher – Tammann (VFT)* Parameters for the Segmental Relaxations obtained from DS for PEG$_{114}$ and PBLG$_{19}$ homopolymers.

Sample	-log(τ_o/s)	B (K)	T_o (K)	T_g^{DS} (K)
PEG$_{114}$	-12	2570 ± 90	133 ± 4	212 ± 1
PBLG$_{19}$	-12	1265 ± 10	240 ± 1	278 ± 1

*VFT equation: $\tau_{max} = \tau_o e^{B/(T-T_o)}$